Distributed thermal monitoring of lithium ion batteries with optical fibre sensors

DOI 10.1016/j.est.2021.102560
ISSN 2352-152X

Publisher: Elsevier

Journal of Energy Storage 39 (2021) 102560

Contents lists available at ScienceDirect

Journal of Energy Storage

journal homepage: www.elsevier.com/locate/est

Distributed thermal monitoring of lithium ion batteries with optical fibre sensors

Yifei Yu [a,*], Elena Vergori [b], Daniel Worwood [a], Yashraj Tripathy [a], Yue Guo [a,c], Aurelio Somá [b], David Greenwood [a], James Marco [a]

[a] WMG, University of Warwick, Coventry, CV4 7AL, UK
[b] Politecnico di Torino – Dipartimento di Ingegneria Meccanica e Aerospaziale, Corso Duca degli Abruzzi, 24, 10129 Torino, Italy
[c] Institute for Future Tranport and Cities, Coventry University, Coventry, CV1 5FB, UK

ARTICLE INFO

Keywords:
Li-ion battery instrumentation
Li-ion battery characterisation
Fibre sensor
Battery thermal management
Distributed temperature monitoring
Li-ion battery performance

ABSTRACT

Real-time temperature monitoring of li-ion batteries is widely regarded within the both the academic literature and by the industrial community as being a fundamental requirement for the reliable and safe operation of battery systems. This is particularly evident for larger format pouch cells employed in many automotive or grid storage applications. Traditional methods of temperature measurement, such as the inclusion of individual sensors mounted at discrete locations on the surface of the cell may yield incomplete information. In this study, a novel Rayleigh scattering based optical fibre sensing technology is proposed and demonstrated to deliver a distributed, real-time and accurate measure of temperature that is suitable for use with Li-ion pouch cells. The thermal behaviour of an A5-size pouch cell is experimentally investigated over a wide range of ambient temperatures and electrical load currents, during both charge and discharge. A distributed fibre optical sensor (DFOS) is used to measure both the in-plane temperature difference across the cell surface and the movement of the hottest region of the cell during operation, where temperature difference is the difference of temperature amongst different measuring points. Significantly, the DFOS results highlight that the maximum in-plane temperature difference was found to be up to 307% higher than that measured using traditional a thermocouple approach.

1. Introduction

Rechargeable lithium-ion batteries (LiB) are extensively employed to underpin the design of energy storage systems (ESS) for use within the automotive and wider electrical generation sector, due to their relatively high gravimetric energy density, power density and low financial cost. It is predicted by many different international organizations that approximately 60% of the total global passenger car market will be electrified by 2050 [1]. Other national reports reinforce this view and forecast a significant shift in the global automotive powertrain mix towards greater levels of electrification, where the combined global market share for EVs, Plug-in hybrid electric vehicles (HEVs) and HEVs may exceed 30% by 2030 [2].

Real-time temperature monitoring of Li-ion batteries is widely regarded within the both the academic literature and by industry as being a fundamental requirement for the reliable and safe operation of battery systems. Traditional methods of temperature measurement, such as the inclusion of individual sensors mounted at discrete locations on the surface of the cell may yield incomplete information. This has implications for cell characterization, when temperature measurements are performed within a laboratory and for the battery management system (BMS) that relies on an accurate measure of temperature to manage battery performance, degradation and safety.

With respect to LiB characterisation, a number of recent publications discuss the experimental evaluation of LiBs for a range of different end-use applications. The nature of the experimental programme employed and associated methodology is often domain specific, but frequently can be traced back to a subset of International Standards, for example those reported within [3]. Such tests involve quantifying the impedance and energy capacity of the battery for a range of load currents and environmental conditions. As reported within [4,5] a number of critical battery parameters are known to vary as a function of cell temperature. As a result, an accurate measure of cell temperature, underpins many of the laboratory experiments that are a pre-requisite to quantifying LiB performance and expected life.

* Corresponding author.
E-mail address: yifei.yu.1@warwick.ac.uk (Y. Yu).

https://doi.org/10.1016/j.est.2021.102560
Received 25 November 2020; Received in revised form 1 March 2021; Accepted 12 April 2021
Available online 29 April 2021

Nomenclature

e	mathematical constant that is the base of the natural logarithm
E	relative change in amplitude, V/m
i	imaginary term
K	temperature calibration constant, °C-1
T	Temperature, °C
z	distance, m
c	speed of light, m/s

Greek symbols

ρ	amplitude of the electrical field, V/m
γ	optical frequency tuning speed, Hz/m
σ	electrical field, V/m
ϕ	phase, °
ω	frequency, Hz

Subscripts and Superscripts

0	initial signal at laser
Coef	calibration coefficient
coupler	scattering signal measured at OC
FUT	Fibre Under Test
l	linear fit
q	quadratic fit
sum	beating signal at OC
T	temperature

Abbreviation

BMS	battery management system
BTMS	battery thermal management systems
CC	constant current
C—OFDR	coherent-optical frequency domain reflectometry
CV	constant voltage
DAQ	data acquisition
DFOS	distributed fibre optic sensor
ESS	energy storage system
EV	electric vehicle
FBG	fibre Bragg grating
FUT	fibre under test
HEV	hybrid electric vehicle
$Li(NiCoMn)O_2$	lithium nickel cobalt manganese oxide
LiB	lithium-ion battery
$LiCoO_2$	lithium cobalt oxide
$LiFePO_4$	lithium iron phosphate oxide
LiPF6	Lithium hexafluorophosphate
$LiMn_2O_2$	lithium manganese oxide
$LiNiO_2$	lithium nickel oxide
LiV_2O_3	lithium vanadium oxide
NMC	Nickel Manganese Cobalt
OC	optical coupler
ODiSI	Optical Distributed Sensor Interrogators
OFDR	optical frequency domain reflectometry
PD	photo detector
PRT	platinum resistance thermometer
RTD	resistance temperature detector
SoC	State of Charge
SoH	State of Health
TC	thermocouple
TLS	tunable laser source

Within many application domains, such as within EVs and HEVs, it is widely accepted that the degradation rate of the ESS and its performance are affected by its operating temperature [6–8] resulting in the need for battery thermal management systems (BTMS) [4] to control the temperature to be within optimal and safe limits. Correct operation of the BTMS typically requires real-time temperature monitoring of the cell surface(s) to determine the required cooling or heating duties. According to the reliable temperature information, efficient ageing predictions [9,10], self-heating [11,12], electrochemical thermal modelling [13–15] and charging managements [16,17] of LiB could be achieved and significantly benefit the development of ESS. In light of this, monitoring the nature of the evolving hot and cold spots within the LiB pack that may occur during operation [18] is, therefore, imperative to achieve effective operation of the BTMS to maximise the performance and cycle life of the battery [19] and to reduce the risk of thermal runaway [20]. Further, accurate information on the magnitude of the forming temperature differences across the cell surface is of critical importance as it is known that these must be minimised to further reduce the battery ageing rate [21].

Within both a laboratory and final application, the conventional approach to surface temperature measurement of LiBs involves point based temperature monitoring [22,23]. Three device types are widely employed and are often bonded to pre-defined strategic locations, such as on the positive and negative tabs or in the centre of the cell [24]. This includes: thermo-resistive devices [22,25], thermo-junctive devices [20,26], and fibre Bragg grating (FBG) sensors [27,28]. Thermal-resistive devices including thermistors [22,25] and resistance temperature detectors (RTD) [29–31] are devices whose resistance varies as a function of temperature. Thermistors typically have an accuracy of $\pm$ 1 °C and are widely utilised to monitor the surface temperature of cells, for example as discussed within [22] for monitoring cylindrical cells or within [18] for pouch cells. The use of RTDs have been reported for temperature measurements inside and on the surface of a coin-type [29] and pouch cell [30,31]. The particular devices reported within [32,33] were selected because nickel foil has a linear thermal coefficient and a temperature measurement range from −40 °C to 60 °C [33,34]. Thermocouples (TCs) are a typical type of thermo-junctive device. The mode of working is based on the Seebeck effect [35] and have been extensively used to take battery internal and external temperature measurements due to their low cost, robustness, small physical size and temperature measurement range [20,26,36]. FBG as a semi-distributed optical fibre sensor (semi-DFOS) is manufactured by inscribing the Bragg-gratings into specific locations of the optical fibre core yielding a permanent change in refractive index [27]. This type of optical fibre sensor has been applied as an embedded measurement device to measure internal strain and temperature [37], as a means of inferring battery state of charge (SOC) and state of health (SOH) [28,38] FBG methods are often limited by the number of gratings that can be multiplexed into a single fibre.

It is noteworthy that both the magnitude and direction of the temperature difference and the location of the hotspot are known to change as the LiB ages and with variations in electrical loading and overall system design [23]. For example, research has identified that during fast charge events, the centre of the cell may become hottest. Conversely, as the cell ages, the location of the hotspot may migrate towards the positive electrode [39,40]. These points highlight the importance of obtaining a full understanding of the temperature distribution within the cell to underpin both accurate characterisation and in-situ thermal management.

In this study, a Rayleigh scattering based DFOS is utilised as a novel distributed temperature sensor. The DFOS is attached to the surface of a LiB under electrical load. This form of optical fibre sensor is well suited to this application because of its small physical size, passivity and robustness from electromagnetic interference and the relatively harsh environments within a commercial battery assembly, including the

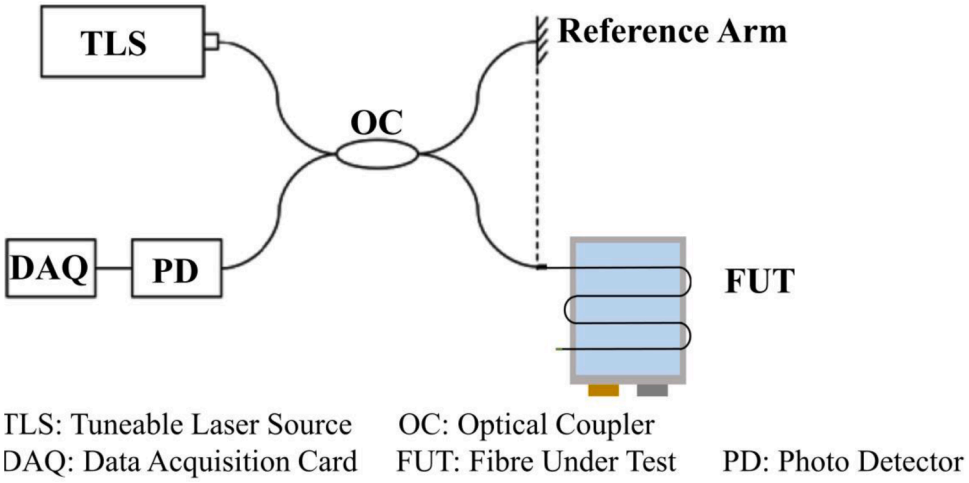

Fig. 1. The simplified configuration of C—OFDR scheme.

possible exposure to highly corrosive electrolyte [28,38]. An optical fibre sensing network based on Rayleigh scattering is deployed to provide a real time and in-situ measurement of the heat generated within an A5-size LiB pouch cell. The suitability of this measurement method is explored through a detailed experimental programme in which the thermal performance of the cell is evaluated for various ambient temperatures and electrical charge and discharge rates.

This paper is divided into six sections. Section two addresses the underpinning theory of a Rayleigh scattering based DFOS. Section three introduces the optical fibre temperature sensor, its calibration and the experimental methodology employed. Section four presents the results from this study and include quantification of the temperature difference and the spatial variation of the hottest cell region for different ambient temperatures and electrical loads. Finally, areas of further work and the conclusions from this study are presented in Sections five and six respectively.

2. Materials and methods

2.1. Theoretical considerations: Rayleigh scattering based DFOS

The theory of Rayleigh scattering results from the interaction of light from non-propagating density fluctuations is discussed within [41,42]. Optical frequency domain reflectometry (OFDR) is one of the schemes employed for high spatial resolution sensing [43]. As discussed within [44,45] Coherent-OFDR is one of the most appropriate means for real-time and in-situ battery temperature monitoring due to its high spatial resolution (circa: in the region of millimetres), temperature accuracy (e.g. ±0.01 °C), measurement repeatability and high measurement bandwidth. The simplified working principle is presented as Fig. 1 for reference.

The simplified configuration of C—OFDR system consists of a tuneable laser source (TLS), an optical coupler (OC), an interferometer which includes a reference arm and a measurement arm, a photo detector (PD) and a data acquisition unit (DAQ). The purpose of utilizing laser source with tuneable frequency is to achieve distributed sensing by pairing location of the sensing point along the FUT and laser output frequency. The optical frequency of the output laser from the TLS is tuned in time to locate distance. The laser splits into two arms after undergoing the OC. The interference light is generated between the reflected light from the reference arm and the Rayleigh backscattering light in the fibre under test (FUT) at the OC. The interference detected by the PD, is in the form of intensity, and then, stored and calculated by the time-frequency analysis [46] in the DAQ to obtain the distributed sensing information.

To simplify the calculation of back-scattered Rayleigh signal, the TLS is assumed to be linearly modulated. The chromatic dispersion and the attenuation effects in all fibres are ignored, and all calculations are considered within the laser coherent length. Similar assumptions are reported in the literature for comparable studies using semiconductor laser source [47]. The electrical field of the output laser from the TLS is given by [48]:

$$\sigma(z) = \rho_0 e^{i\varphi(z)} \tag{1}$$

where ρ_0 is the amplitude of the electrical field from the laser, $\varphi(z)$ is the phase term and can be shown as:

$$\varphi(z) = \int_0^z \omega(z)dz = \int_0^z (\omega_0 + \gamma z)dz = \varphi_0 + \omega_0 z + \frac{1}{2}\gamma z^2 \tag{2}$$

where $\omega(z) = \omega_0 + \gamma z$ is the linear tuning frequency, ω_0 the initial laser frequency, γ is the optical frequency tuning speed, φ_0 is the initial phase.

The reflected signals from the reference arm and the Rayleigh scattering signal from FUT can be shown as:

$$\sigma_{ref0}(z) = \rho_{ref0}(z) e^{i\varphi_{ref0}(z)} \tag{3}$$

$$\sigma_{FUT0}(z) = \rho_{FUT0}\ (z) e^{i\varphi_{FUT0}(z)} \tag{4}$$

where $\sigma_{ref0}(z)$ and ρ_{ref0} are the electric field at the reference arm and the amplitude of it respectively. $\sigma_{FUT0}(z)$ and ρ_{FUT0} are the electrical field at the measurement arm and the amplitude of it, respectively. When the two fields are superimposed at the OC, the amplitude of the scattering signals becomes:

$$\begin{aligned}|\sigma_{sum}(z)|^2 = {} & |\sigma_{FUT0}(z - z_{FUT})|^2 + \left|\sigma_{ref0}\left(z - z_{ref}\right)\right|^2 \\ & + \sigma_{FUT0}(z - z_{FUT})\sigma^*_{ref0}\left(z - z_{ref}\right) + \sigma_{ref0}\left(z - z_{ref}\right)\sigma^*_{FUT0}(z - z_{FUT})\end{aligned} \tag{5}$$

This equation reveals that the resultant signal that is mixed by the signal scattered from FUT and signal from the reference arm at OC, $|\sigma_{sum}(z)|^2$, is highly correlated to both the original FUT and reference fibre scattering patterns. When a cross-correlation is performance between scattering from the FUT and resultant signal at OC, a peak in amplitude will occur at $z = z_{FUT}$, locating the FUT segment. The value of z_{FUT} can be extracted from the frequency spectrum through application of a fast Fourier transform (FFT). By utilising a laser source with a linear tuning frequency, the resultant frequency of $\sigma_{ref0}(z)$ and $\sigma_{FUT0}(z)$ at OC is proportional to the length of the FUT, realizing the distributed optical fibre sensor along the entire length.

In the case of temperature measurement, if the temperature along the length of the FUT changes, this will impose a slowly varying envelope (in

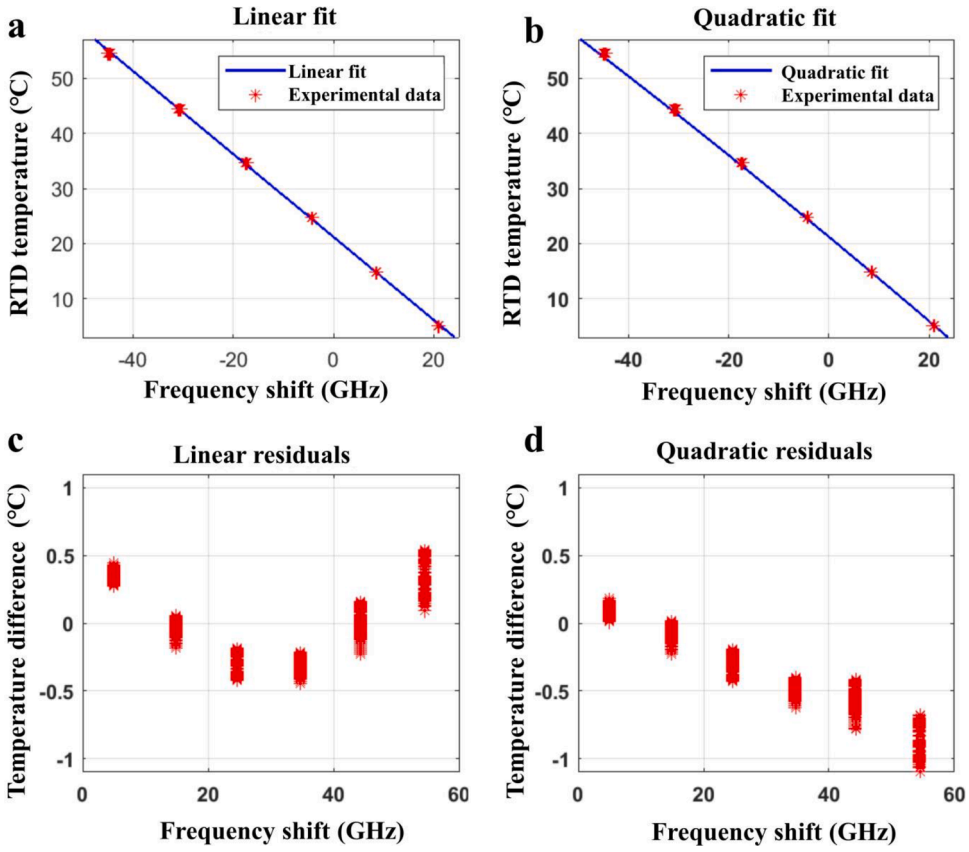

Fig. 2. Temperature as a function of frequency shift, with a linear a) and quadratic b) fit applied to 100 raw experimental measurements. Temperature difference between measured and fit results, as a function of frequency shift, using linear c) and quadratic fit d).

term of phase) upon the backscattering from that segment of FUT. The scattering signal measured at OC will have the form:

$$\sigma_{coupler}(z) = E_{FUT}(z)\rho_{FUT0}(z)e^{i\varphi_{FUT0}(z)+i\delta_{FUT}(z)} + \rho_{ref0}(z)e^{i\varphi_{ref0}(z)} \tag{6}$$

Where E and δ represent the relative change in amplitude and phase between the original data sets and the newly measured data. If multiply $\sigma_{coupler}(z)$ by the complex conjugate of the scattering signal from the FUT, $\sigma_{FUT0}(z)$, shifted by the appropriate amount to align with the fibre segment in the new data set, a new equation can be derived:

$$\sigma_{coupler}(z)\sigma^{*}_{FUT0} = \rho^{2}_{FUT0}E_{FUT}(z)e^{i\delta_{FUT}(z)} + \rho_{FUT0}(z)\rho_{ref0}(z)e^{i\varphi_{ref0}(z)-i\varphi_{FUT0}(z)} \tag{7}$$

By averaging the data produced using Eq. (7) over a large number of points, the amplitude and phase information along the FUT can be evaluated.

$$\begin{aligned}\left\langle\left[\sigma_{FUTx}(z)+\sigma_{refx}(z)\right]\sigma^{*}_{FUT0}(z)\right\rangle &= \left\langle\rho^{2}_{FUT0}(z)\right\rangle\left\langle E_{FUT}(z)\right\rangle\left\langle e^{i\delta_{FUT}(z)}\right\rangle \\ &= \left\langle\rho^{2}_{FUT0}\right\rangle E_{FUT}e^{i\langle\delta_{FUT}\rangle}\end{aligned} \tag{8}$$

Accordingly, if there is a section of the FUT that has been heated or cooled, the scattering amplitude will be largely unaffected. Instead, the phase term will accumulate a linearly growing difference due to the thermo-optic effect [45]. The rate of change of the phase data can therefore be used as an indicator of the rate of temperature change. This underpins the theory behind Rayleigh scattering based C—OFDR system [45]. In conventional Rayleigh scattering, the whole fibre can be regarded as a composition of thousands or millions of FBGs. The phase shift of sensing segment thus can be calculated by transforming the spatial domain signal to optical frequency domain signal in the OFDR system, which is referred as Rayleigh back-scattering spectra [46,49] This localised phase shift is represented by a frequency shift in the Luna ODiSI system to form a distributed temperature sensor. This system can deliver a distributed temperature measurement from −40 °C to 220 °C with 2.6 mm spatial resolution and <0.1 °C temperature resolution and ±0.01 °C repeatability.

2.2. Optical fibre temperature sensor

The optical fibre employed in this study is a polyimide coated, low bend loss, single mode fibre (SMF). The physical length and index of refraction of the fibre are intrinsically sensitive to the measurement of both temperature and strain. During experimentation, the optical fibre is contained within a Poly-Tetra-Fluoro-Ethylene (PTFE) tube, thereby ensuring the fibre is not affected by mechanical strain and the resultant measurement is solely a function of variations in temperature.

2.3. Temperature calibration

As defined by Eq. (9), a change in the measured temperature, results in a phase shift in the spectrum of light scattering within the FUT. This thermal response arises due to the inherent thermal expansion of the fibre material and the temperature dependence of the refractive index. In the absence of any mechanical strain, the temperature change ΔT is defined as:

$$\Delta T = -\frac{\overline{\lambda}}{cK_T}\Delta\nu \tag{9}$$

Where $\overline{\lambda}$ defines the centre wavelength of the scan, c the speed of light, K_T the temperature calibration constant, and $\Delta\nu$ is the measured shift in frequency. The distributed measure of temperature along the FUT is copies of the frequency shift distribution multiplied by the coefficient $T_{coef} = \frac{\overline{\lambda}}{cK_T}$ with units of °C/GHz. For the purpose of sensor calibration, the optical fibre was bonded with epoxy resin to an aluminium bar. A

Table 1
Experimental data measured by PRT and optical fibre.

Chamber temperature (°C)	5.00	15.00	25.00	35.00	45.00	55.00
Measured PRT value (°C)	5.03	14.85	24.70	34.65	44.36	54.54
Measured DFOS mean (GHz)	21.01	8.49	−4.25	−17.43	−30.76	−44.70
Measured DFOS variance (GHz)	0.00	0.00	0.01	0.00	0.01	0.02
Calculated DFOS output (linear fit) (°C)	5.38	14.81	24.40	34.33	44.36	54.86
Calculated DFOS output(quadratic fit) (°C)	5.04	14.87	24.67	34.61	44.44	54.50

platinum resistance thermometer (PRT), was placed using Kapton tape in close physical proximity to the optical fibre. The PRT, is able provide a temperature measurement with an accuracy of ±0.15 °C.

The calibration procedure employed was: (1) the calibration set-up was placed into a thermal chamber; (2) the data acquisition system for the DFOS was set to record measurements of frequency shift and the temperature output from the PRT; (3) the temperature of the thermal chamber was set from 5 to 55 °C with 10 °C incremental steps. At each temperature increment, the thermal chamber was allowed to reach thermal equilibrium. Within the context of this experiment, this is defined as the output from the PRT changing less than ±0.15 °C over a 20 min time period. Once thermal stability has been achieved, 100 measurements were taken and the arithmetic mean and variance calculated. Fig. 2a and b show the mean value recorded for each temperature region with both a linear and quadratic fit through the data points. Fig. 2c and d presents the residuals of the linear and quadratic fit respectively.

Table 1 presents the output from the PRT sensor and the optical fibre. The results indicate that for temperature tests undertaken in the range: 5 °C - 55 °C with the polyimide coated FUT, a linear fit with coefficient −0.753 °C/GHz, results in a 0.273 °C measurement deviation calculated by the 100 raw experimental measurements. Conversely, a quadratic fit

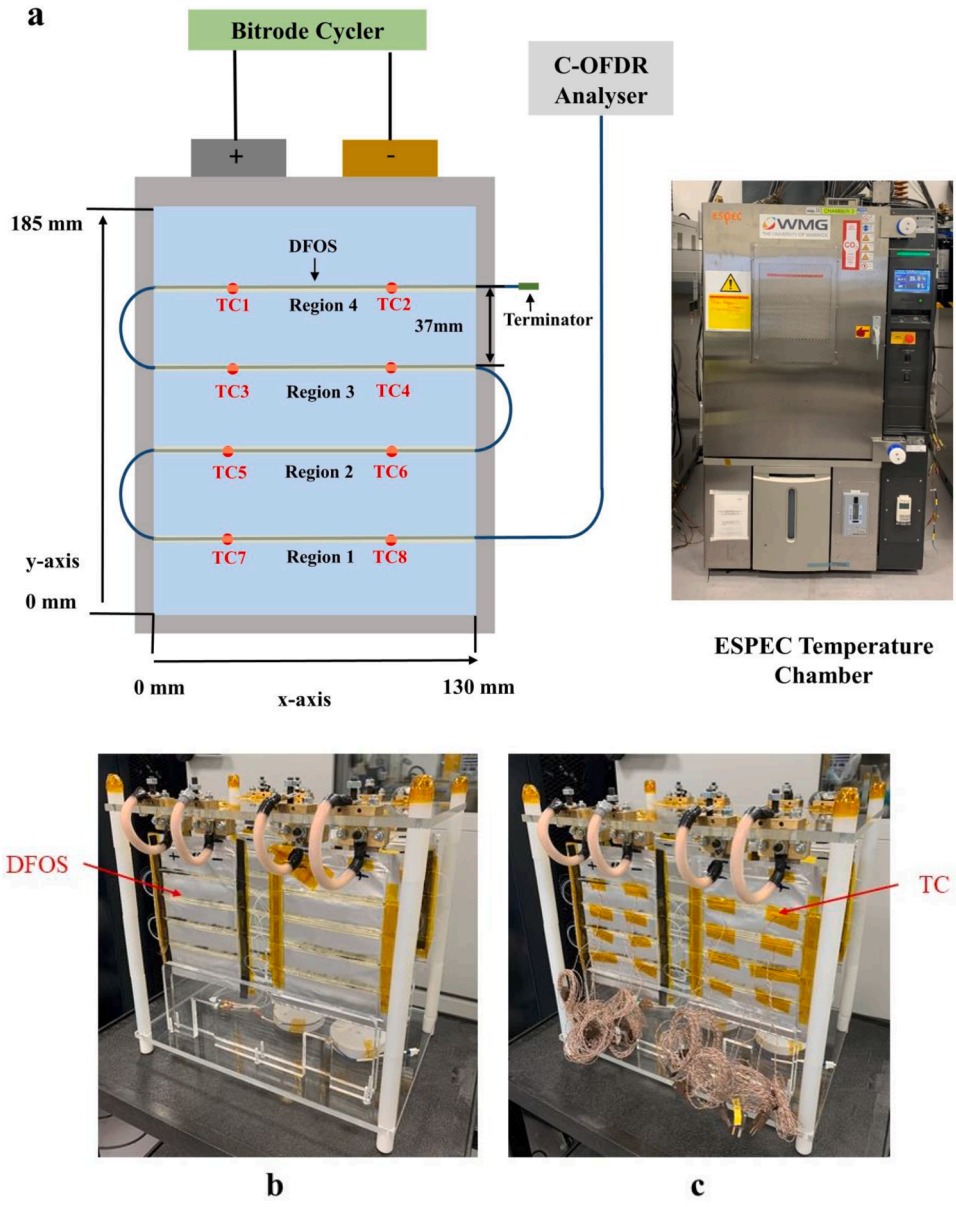

Fig. 3. a) Schematic of pouch cell test setup with the locations of DFOS and TCs. Images of b) test rig with DFOS instrumented A5-size pouch cells; c) assembled test rig with DFOs and thermocouples.

Table 2
Battery test procedure.

Chamber Temperature	Step No.		Parameters			Limits			
		Action	Quantity	Value	Unit	Quantity		Value	Unit
10, 25 and 40 °C	1	REST				Step time	=	60	min
	2	CHARGE	Current	5	A				
			Voltage	4.2	V	Current	<=	0.25	A
	3	REST				Step time	=	30	min
	4	DISCHARGE	Current	5	A	Voltage	<=	2.5	V
	5	REST				Step time	=	30	min
	6	CHARGE	Current	15	A				
			Voltage	4.2	V	Current	<=	0.25	A
	7	REST				Step time	=	30	min
	8	DISCHARGE	Current	15	A	Voltage	<=	2.5	V
	9	REST				Step time	=	30	min
	10	CHARGE	Current	25	A				
			Voltage	4.2	V	Current	<=	0.25	A
	11	REST				Step time	=	30	min
	12	DISCHARGE	Current	25	A	Voltage	<=	2.5	V
	13	REST				Step time	=	180	min

with first and second order coefficients of −0.767 °C/GHz and −0.000602 °C/GHz^2 results in a 0.502 °C deviation. Derivation of the temperature output from the optical form fibre is obtained through Eqs. (10) and (11) respectively. The terms T_l and T_q define the temperature change for the linear and quadratic fit respectively and $\Delta\nu$ is the value of frequency shift. Based on the results presented in Fig. 2, Table 1 and measurement deviation, the linear fit for calculating temperature from the DFOS is subsequently employed in Section 3.

$$T_l = -0.753\Delta\nu + 21.202 \tag{10}$$

$$T_q = -0.000602\Delta\nu^2 - 0.767\Delta\nu + 21.421 \tag{11}$$

2.4. Experimental set-up

A schematic diagram of the experimental setup, for deploying the DFOS to measure the surface temperature of an A5-size LiB pouch cells is

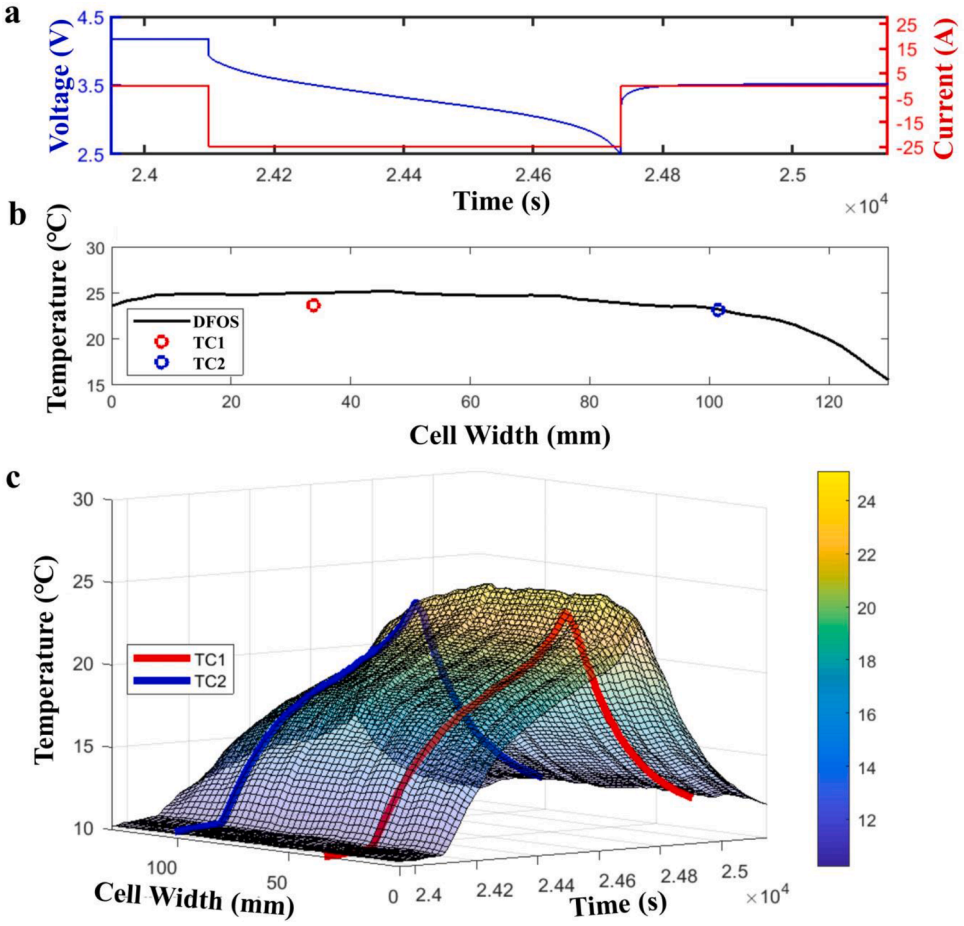

Fig. 4. Comparison between the temperature measured by DFOS and TCs over time evolution of 5C discharge at 10 °C ambient temperature. a) Voltage and current measurement of 5C. b) Instantaneous temperature measured by DFPS and TCs. c) Temperature evolution measured by DFOS and TCs.

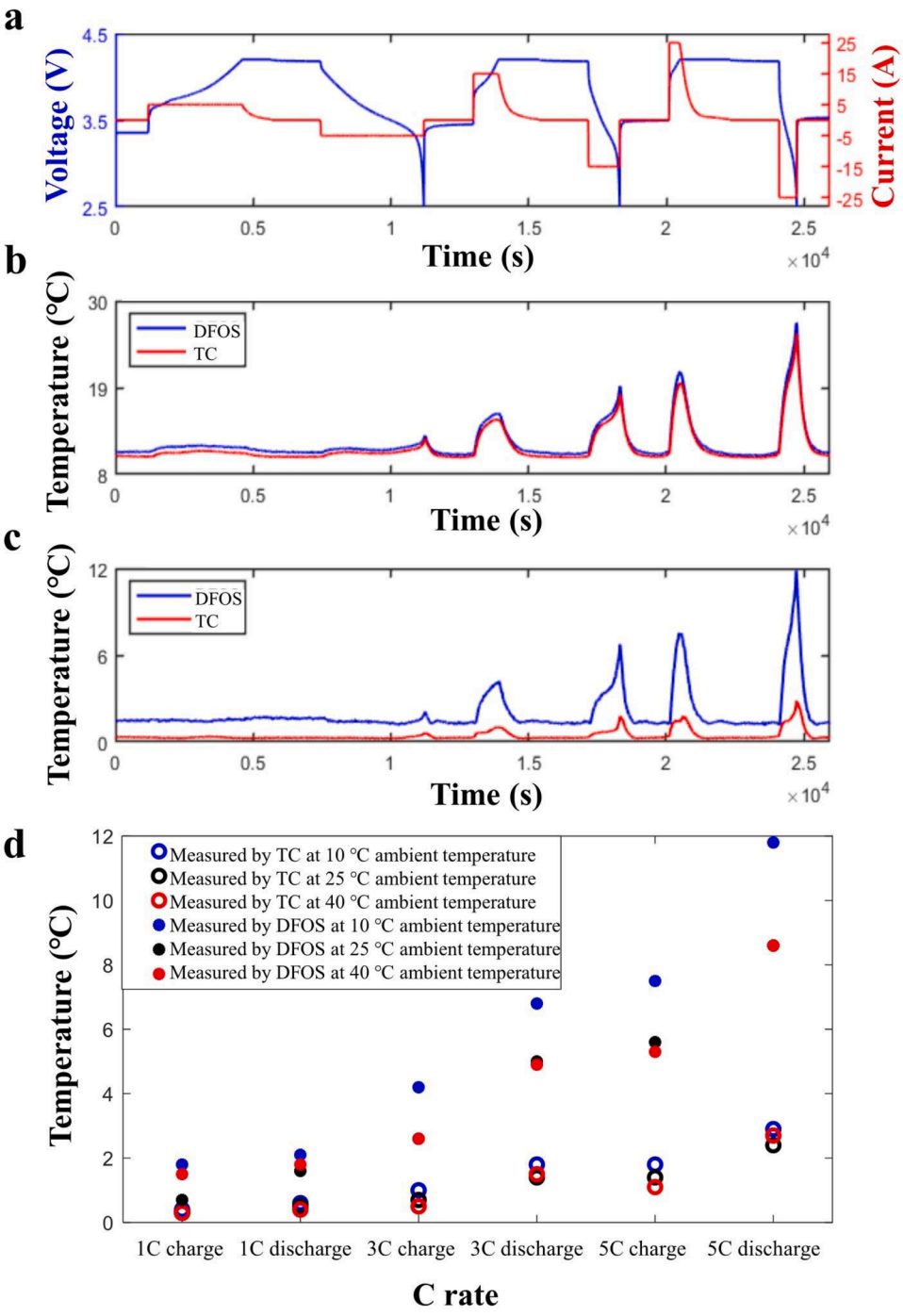

Fig. 5. a) Electrical load profile, b) Synchronized maximum temperature and **c**) In-plane temperature difference measured by TCs and DFOS at 10 °C ambient temperature during 1, 3 and 5C charge and discharge operations. **d**) Maximum in-plane temperature difference measured by DFOS and TCs during 1, 3 and 5C charge and discharge at 10, 25 and 40 °C ambient temperatures, where data measured by DFOS during 3C charge and 5C discharge at 25 and 40 °C ambient temperatures are superposed.

shown in Fig. 3a. The LiB comprises of 8 layers of graphite anode with 330 mAh/g material capacity, 7 layers of Nickel Manganese Cobalt (NMC) with 150 mAh/g material capacity, with Lithium hexafluorophosphate (LiPF6) electrolyte. The resulting cell has a 5 Ah nominal energy capacity with a nominal voltage of 3.6 Vage. A 5 m long DFOS was bonded to the surface of the pouch cell using epoxy glue and 8 TCs were attached using Kapton tape to side 1 of the cell at predefined locations (TC1-TC8) to validate the output of the DFOS. The response of the DFOS was measured by a Luna ODiSI B operating at 23.5 Hz with a spatial resolution along the length of the FUT of 1.3 mm. The measurement of TCs were collected by the Pico Data Logger. A Bitrode cycler was used to charge and discharge the LIB under test. The output voltage from the cycler is 5 V with a current measurement resolution of 0.001 Amps. During experimentation, all LiBs were placed inside an Espec temperature chamber to facilitate a controllable ambient temperature and to ensure safe operation of the experiment.

In order to achieve a more uniform air flow across all surfaces of the LiB, each cell was suspended from the rig ceiling by their tabs, as shown in Fig. 3b and c, in which each tab is connected to brass conduction blocks. Fig. 3b), shows four pouch cells instrumented on both sides with two 5 m long DFOS. Conversely, Fig. 3c shows the assembled test rig with the inclusion of additional TCs (TC1-TC8) and those required to underpin operation of the Bitrode cycler. The TCs applied in this study are T-type with a measurement accuracy of ±1 °C. Comparing Fig. 3b and 3c further highlights the reduced complexity of the experimental set-up using DFOS to provide a distributed measure of cell surface temperature as opposed to a number individual point measurement devices; each requiring their own signal connection and electrical wiring

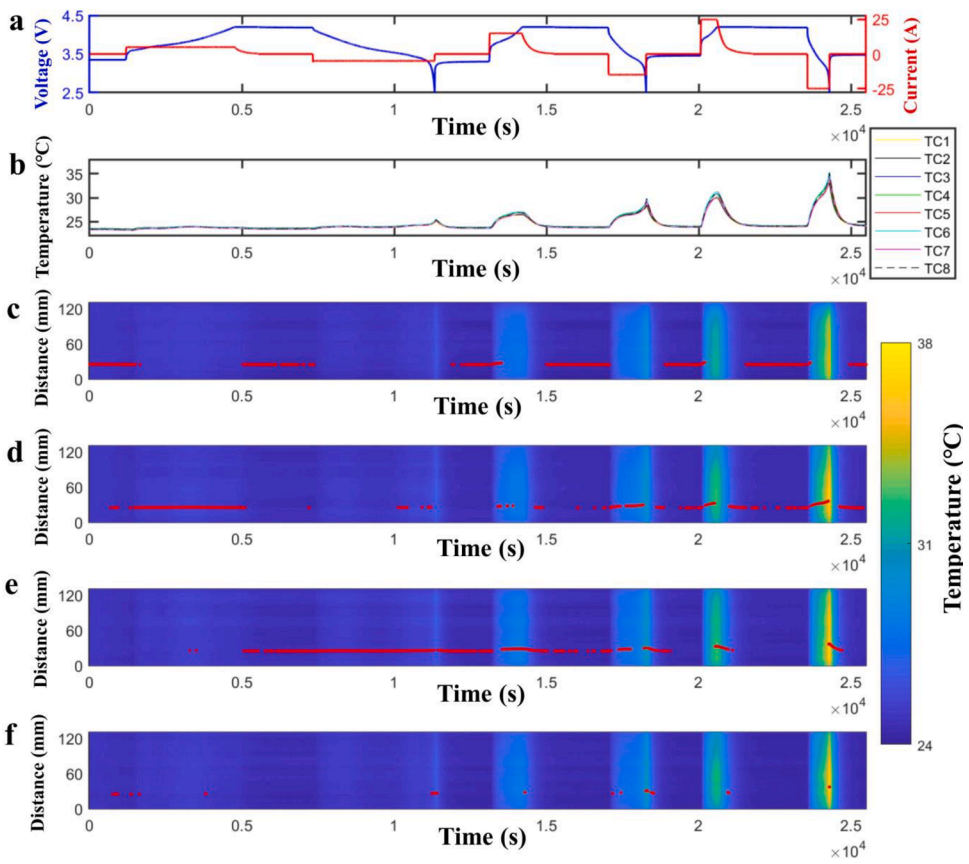

Fig. 6. CCCV Charging and CC discharging over time revolution at 25 °C ambient temperature with cell surface temperature measured by DFOS and TC over a time revolution of 1, 3 and 5C charge and discharge, where the red dot along time domain is the instantaneous maximum temperature of a surface measured by DFOS. a). Current and voltage evolution. b) Temperature measured by TC. c) Temperature and hotspot measured by DFOS at region 4. d) Temperature and hotspot measured by DFOS at region 3. e) Temperature and hotspot measured by DFOS at region 2. f) Temperature and hotspot measured by DFOS at region 1 at 25 °C ambient temperature.

for data acquisition and cycler control.

2.5. LiB test procedure

Table 2 summarises the experimental procedure employed. The electrical cycling of the battery, defined in Table 2, was repeated for three ambient temperatures (10, 25 and 40 °C). When the ambient temperature of the LiBs was modified, the batteries was rested at the target temperature for 180 min to reach thermal equilibrium before electrical loading commenced. As it can be seen from Table 2, each cell is charged using a constant current-constant-voltage (CC—CV) procedure. Charge and discharge rates of 1C, 3C and 5C were employed respectively. For each CC charge phase, cells were charged to the upper voltage of 4.2 V. Cells were held at 4.2 V until the charge current reduced below C/20 amps at which point the cells were allowed to rest for 30 min. For discharge, a CC current was applied to the cell until a cut-off voltage of 2.5 V was reached. A further rest period of 30 min was applied before commencing the next charge-discharge cycle at the higher C-rate, where C-rate is a measure of the rate at which a battery is discharged relative to its maximum capacity.

3. Results and discussion

3.1. Definition of temperature difference

Fig. 4 highlights the measured evolution of surface temperature along the width of the cell, for a 5C discharge at an ambient temperature of 10 °C, as an example to illustrate surface temperature measured by DFOS and TCs. By investigation of the data captured by 8 TCs and 4 regions of DFOS, the maximum in-plane temperature difference measured by the DFOS reaches a value of 11.8 °C during the 5C discharge, where the lowest surface temperature is 15.5 °C and the highest is 27.2 °C. However, the maximum in-plane temperature difference measured by the TCs is 2.9 °C. An underestimation of 307%. The reasons for this discrepancy are primarily because of the limited measurement locations of TCs compared with the measurement capability of the distributed optical fibre sensor. Conversely from the DFOS, the variation in temperature follows a non-linear curvature, with a peak occurring spatially between the two TCs.

This phenomena can be observed further in Fig. 5a, b and c, where the magnitude of the in-plane temperature difference increases at higher C-rate cycling due to the higher rate of cell heat generation. By collecting the maximum in-plane temperature difference measured by the DFOS and TCs at 10, 25 and 40 °C ambient temperatures, it can be seen that in-plane temperature difference increases when the electrical loads were varied from 1C to 5C. Both the amplitude and difference of maximum in-plane temperature difference measured by the DFOS is higher than that measured by TCs, which demonstrates that DFOS can capture more thermal difference information compared with TCs. This is shown in Fig. 5d, where it is observed that the point based TC underestimate the magnitude of the in-plane temperature difference relative to the DFOS. The magnitude in temperature difference underestimation is more pronounced as the cell C-rate increases, which further highlights the issue of conventional real time monitoring for high performance applications.

3.2. Definition of the cell hot spot location

As discussed in Section 1, the anisotropic thermal properties of a LiB imply that the level of heat generation across of the surface of the cell is not uniform. As a result, the hottest location on the cell surface (i.e. the hot spot) is known to vary during the charge and discharge process. Fig. 6 presents the variation in surface temperature across each region (1, 2, 3 and 4) as the cell is electrically loaded at an ambient temperature of 25 °C. The red dots in this figure, highlight the maximum instantaneous temperature on the cell surface and shows graphically how the location of the hotspot moves across the width of the cell (x-axis) and

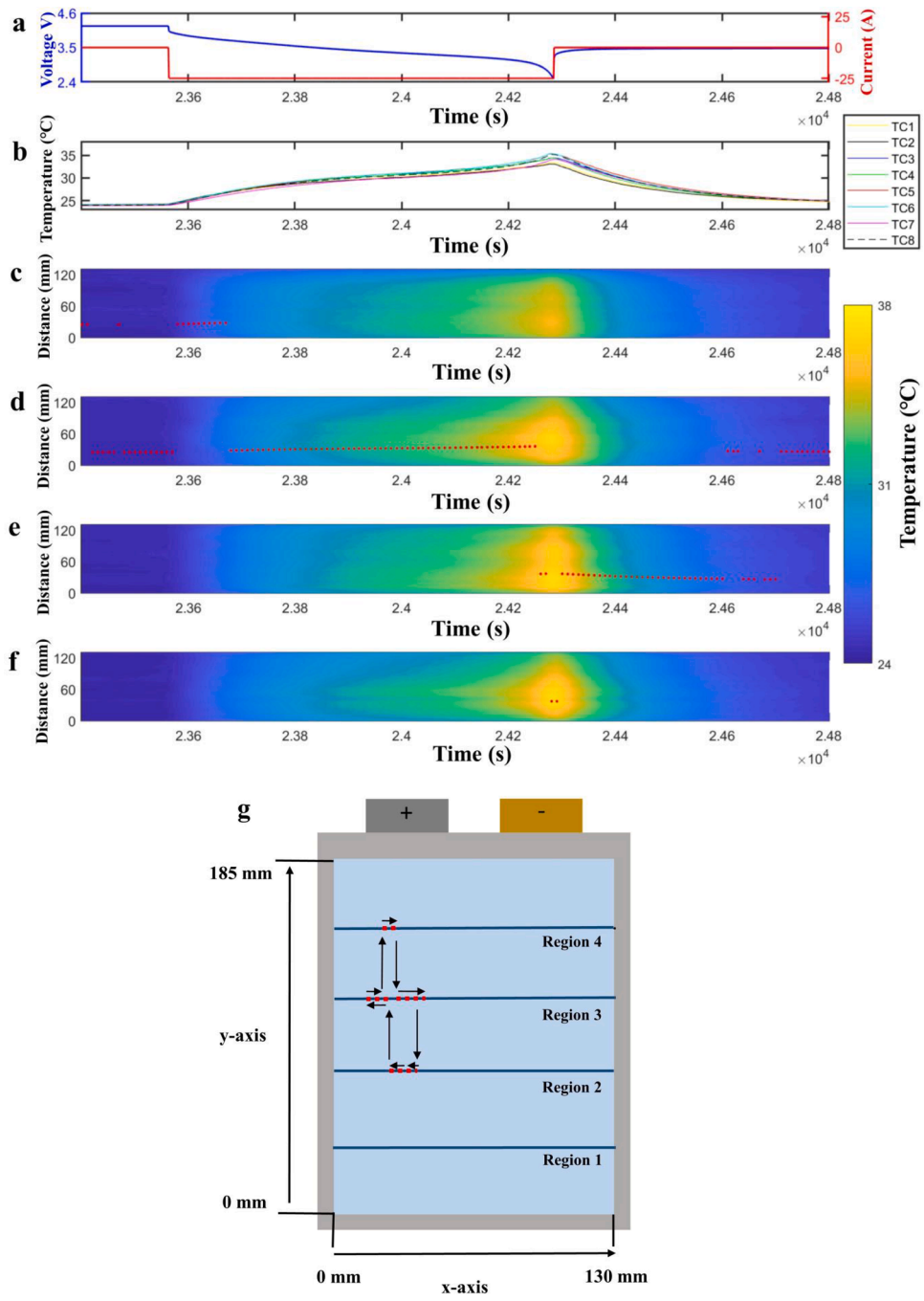

Fig. 7. 5C discharge at 25 °C ambient temperature with cell surface temperature measured by DFOS and TC over a time revolution, where the red dot along time domain is the instantaneous maximum temperature of a surface measured by DFOS. a). current and voltage evolution. b) Temperature measured by TC. c) Temperature and hotspot measured by DFOS at region 4. d) Temperature and hotspot measured by DFOS at region 3. e) Temperature and hotspot measured by DFOS at region 2. f) Temperature and hotspot measured by DFOS at region 1 at 25 °C ambient temperature. g) The simplified movement of hotspot during 5C discharge at 25 °C ambient temperature illustrated graphically on the cell surface.

also the y-axis, between the different regions defined in Fig. 3a. From Fig. 6, it can be seen that throughout the charge/discharge process the surface temperature of the cell on the positive terminal side is hottest (e.g. 0 $< x <$ 65 mm). The hottest region of the cell is generally region 2. However, as the C-rate is increased, the hotspot to seen to move around the cell surface primarily within regions 2 - 4. To further understand this phenomena, Fig. 7 presents the region of data for the 5C charge/discharge cycle in greater detail. The hot spot is predominately within region 3 and during charge moves from the edge (x = 24.8 mm) to a more central location (x = 36.1 mm). However, there are significant periods of time, where this is not the case. Towards the end of the discharge, the hot spot moves to region 2 and quickly reaches the maximum temperature, 37.1 °C at 37.1 mm from the edge in region 1 before transitioning back to region 2. During the relaxation period the location of the hotspot remains in region 2 and tends towards the left-hand edge (x = 0 mm) of the cell surface as heat reduces. The simplified movement of the hot spot during the 5C discharge at 25 °C ambient temperature is illustrated graphically on the cell surface in Fig. 7g.

As highlighted by Fig. 8, when the ambient temperature is reduced to 10 °C, the thermal behaviour of the LiB is different, in that the hot spot locations are mainly distributed in region 4 of the cell. During all of the relaxation stages when no current is flowing, the hot spots are measured in region 4 at locations from $x = 10.7$ to $x = 10.9$ mm. For a 1C discharge to 5C discharge electrical loading, the hot spot moves along the Z-axis, with a peak at 25.9 °C during the 5C discharge at a location of $x = 27.2$ mm within region 3. Comparing Figs. 6 and 8, the results highlight that the physical location and movement of the hotspot is altered not only by the magnitude of the electric load, but also by the ambient temperature. These results are consistent with those published in [24] and further demonstrate the potential limitation of using individual TCs to

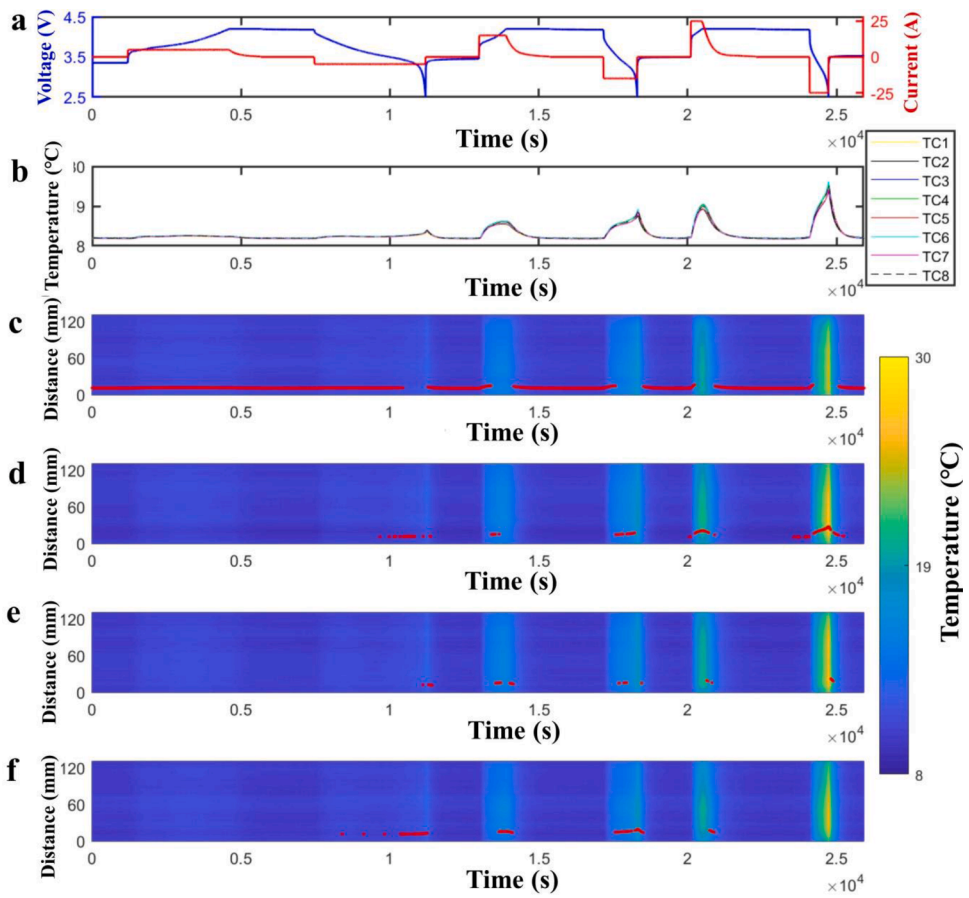

Fig. 8. CCCV Charging and CC discharging over time revolution at 10 °C ambient temperature with cell surface temperature measured by DFOS and TC over a time revolution of 1, 3 and 5C charge and discharge, where the red dot along time domain is the instantaneous maximum temperature of a surface measured by DFOS. a) Current and voltage evolution. b) Temperature measured by TC. c) Temperature and hotspot measured by DFOS at region 4. d) Temperature and hotspot measured by DFOS at region 3. e) Temperature and hotspot measured by DFOS at region 2. f) Temperature and hotspot measured by DFOS at region 1 at 10 °C ambient temperature.

understand the thermal behaviour of a LiB under electrical excitation at different ambient temperatures.

4. Future work

Areas of further work from this study are defined below within the context of both LiB characterization and integration with the BMS. To understand the transferability of these results, the experimental programme defined in Section 2, will be repeated on different cell chemistries and formats. Of particular interest is the use of larger format pouch cells, such as those described in [51], where the occurrence of temperature differences is reported as being a challenge for the design of the thermal management solution. With application of the DFOS on a single side of the pouch cell, it is only possible to quantify the in-plane temperature differences. Further experimental research will apply the DFOS on both cell surfaces facilitating the simultaneous measurement of the in-plane and cross-plane temperature differences. The latter is discussed within [21] as being important with pouch cells that contain a large number of internal layers, each connected electrically in parallel. Further work also includes optimizing the pattern and location of the DFOS over the cell surface and the cell tab; the objective being to minimize the length of the DFOS while maintaining the highest level of measurement accuracy and resolution. Moreover, the relationship between the changes of hot spot location with respect to the ageing state of LiB will be investigated in the future work. Research is ongoing to insert the DFOS within the LiB to yield an accurate measure of internal temperature. Key to this research is a robust methodology for instrumented cell manufacture and confirmation that DFOS insertion does not negatively impact LIB performance or life. Within the context of BMS integration, research is underway to design bespoke electronics hardware to perform in-situ OFDR operation. The electronics may be integrated with the BMS hardware or be installed within the final application and communicate with the BMS via an appropriate network technology, such as a Controller Area Network or Serial Peripheral Interface.

5. Conclusions

Within this study, a novel Rayleigh scattering based optical fibre sensing technology is proposed and demonstrated to deliver a distributed, real-time and accurate measure of temperature that is suitable for use with li-ion pouch cells. A DFOS is used to measure both the in-plane temperature difference across the cell surface and the movement of the hottest region of the cell during operation. Experimental results highlight that the use of DFOS provides a comparable level of accuracy, relative to TCs, but the significantly increased spatial resolution of the measurement over the surface of the cell, yields a greater understanding into the in-plane temperature difference and the location of the hotspot. Significantly, the DFOS results highlight that the maximum in-plane temperature difference of 11.8 °C occurs at an ambient temperature 10 °C during a 5C discharge. This was found to be up to 307% higher than that measured using traditional a thermocouple approach. Further, the results show that the location of the LIB hot spot is a function of both excitation current and ambient temperature and therefore will vary during operation. Being able to measure and identify both attributes within a laboratory or BMS application will help underpin improved LiB management and improved design of the thermal management system leading to reduced degradation and improved safety.

CRediT authorship contribution statement

Yifei Yu: Conceptualization, Methodology, Data curtion, Writing – original draft, Visualization, Investigation, Writing – review & editing.

Elena Vergori: Conceptualization, Methodology, Data curtion. **Daniel Worwood:** Writing – review & editing. **Yashraj Tripathy:** Investigation, Formal analysis. **Yue Guo:** Conceptualization. **Aurelio Somá:** Conceptualization. **David Greenwood:** Conceptualization, Supervision, Resources. **James Marco:** Conceptualization, Investigation, Supervision, Writing – review & editing.

Declaration of Competing Interest

The authors declare that they have no known competing financial interests or personal relationships that could have appeared to influence the work reported in this paper.

Acknowledgement

This work was funded by the EPSRC (Engineering and Physical Sciences Research Council), grant reference EP/R004927/1, titled 'Prosperity Partnership'.

References

[1] A. Barré, B. Deguilhem, S. Grolleau, M. Gérard, F. Suard, D. Riu, A review on lithium-ion battery ageing mechanisms and estimations for automotive applications, J. Power Sources 241 (2013) 680–689.
[2] Goldman Sachs Global Investment Research, "Electric vehicle boom : iCE-ing the combustion engine," 2017.
[3] D. I. Idaho National Laboratory, *battery test manual for plug-in hybrid electric vehicles*, INL/EXT-07. Idaho Falls, Idaho 83415, 2010.
[4] C. Menale, F.D. Annibale, B. Mazzarotta, R. Bubbico, Thermal management of lithium-ion batteries : an experimental investigation, Energy 182 (2019) 57–71.
[5] M. Cabanero, J. Altmann, L. Gold, N. Boaretto, J. Muller, S. Hein, J. Zausch, J. Kallo, A. Latz, Investigation of the temperature dependence of lithium plating onset conditions in commercial Li-ion batteries, Energy 171 (2019) 1217–1228.
[6] L. Gu, J. Yupeng, J.V. Wang, G. Zhu, J. Kang, Parameterized evaluation of thermal characteristics for a lithium-ion battery, Energy 178 (2019) 21–23.
[7] J. Wu, Z. Wei, K. Liu, Z. Quan, Y. Li, Battery-involved energy management for hybrid electric bus based on expert-assistance deep deterministic policy gradient algorithm, IEEE Trans. Veh. Technol. 69 (11) (2020) 12786–12796.
[8] J. Wu, Z. Wei, W. Li, Y. Wang, Y. Li, D. Sauer, battery thermal- and health-constrained energy management for hybrid electric bus based on soft actor-critic DRL algorithm, IEEE Trans. Ind. Inf. 3203 (2020).
[9] K. Liu, Y. Li, X. Hu, M. Lucu, W.D. Widanage, Gaussian process regression with automatic relevance determination kernel for calendar aging prediction of lithium-ion batteries, IEEE Trans. Ind. Inf. 16 (6) (2020) 3767–3777.
[10] X. Tang, K. Liu, X. Wang, F. Gao, J. Macro, W.D. Widanage, Model migration neural network for predicting battery aging trajectories, IEEE Trans. Transp. Electrif. 7782 (c) (2020) 1–12.
[11] Y. Shang, K. Liu, N. Cui, N. Wang, K. Li, C. Zhang, a compact resonant switched-capacitor heater for lithium-ion battery self-heating at low temperatures, IEEE Trans. Power Electron. 35 (7) (2020) 7134–7144.
[12] Y. Shang, K. Liu, N. Cui, Q. Zhang, C. Zhang, A Sine-wave heating circuit for automotive battery self-heating at subzero temperatures, IEEE Trans. Ind. Inf. 16 (5) (2020) 3355–3365.
[13] V.G. Choudhari, A.S. Dhoble, S. Panchal, Numerical analysis of different fin structures in phase change material module for battery thermal management system and its optimization, Int. J. Heat Mass Transf. 163 (2020), 120434.
[14] M.S. Patil, J.H. Seo, S. Panchal, M.Y. Lee, Numerical study on sensitivity analysis of factors influencing liquid cooling with double cold-plate for lithium-ion pouch cell, Int. J. Energy Res. 45 (2020) 2533–2559.
[15] M.H. Akhoundzadeh, K. Raahemifar, S. Panchal, E. Samadani, E. Haghi, R. Fraser, A conceptualized hydrail powertrain: a case study of the Union Pearson Express route, World Electr. Veh. J. 10 (2) (2019) 1–14.
[16] K. Liu, X. Hu, Z. Yang, Y. Xie, S. Feng, Lithium-ion battery charging management considering economic costs of electrical energy loss and battery degradation, Energy Convers. Manag. 195 (February) (2019) 167–179.
[17] M. Abdel-monem, K. Trad, N. Omar, O. Hegazy, P. Van Den Bossche, J. Van Mierlo, Influence analysis of static and dynamic fast-charging current profiles on ageing performance of commercial lithium-ion batteries, Energy 120 (2017) (2020) 179–191.
[18] C. Veth, D. Dragicevic, C. Merten, Thermal characterizations of a large-format lithium ion cell focused on high current discharges, J. Power Sources 267 (2014) 760–769.
[19] H. Liu, Z. Wei, W. He, J. Zhao, Thermal issues about Li-ion batteries and recent progress in battery thermal management systems: a review, Energy Convers. Manag. 150 (May) (2017) 304–330.
[20] G. Vertiz, M. Oyarbide, H. Macicior, O. Miguel, I. Cantero, P. Fernandez, I. Ulacia, Thermal characterization of large size lithium-ion pouch cell based on 1d electro-thermal model, J. Power Sources 272 (2014) 476–484.
[21] I.A. Hunt, Y. Zhao, Y. Patel, J. Offer, Surface cooling causes accelerated degradation compared to tab cooling for lithium-ion pouch cells, J. Electrochem. Soc. 163 (9) (2016) A1846–A1852.
[22] T. Waldmann, G. Bisle, B. Hogg, S. Stumpp, M. Danzer, M. Kasper, P. Axmann, M. Mehrens, influence of cell design on temperatures and temperature gradients in lithium-ion cells : an in operando study influence of cell design on temperatures and temperature gradients in lithium-ion cells : an in operando study, J. Electrochem. Soc. 162 (6) (2016) A921–A927.
[23] Z. Wei, J. Zhao, H. He, G. Ding, H. Cui, L. Liu, Future smart battery and management: advanced sensing from external to embedded multi-dimensional measurement, J. Power Sources 489 (January) (2021), 229462.
[24] T. Grandjean, A. Barai, E. Hosseinzadeh, Y. Guo, A. McGordon, J. Marco, Large format lithium ion pouch cell full thermal characterisation for improved electric vehicle thermal management, J. Power Sources 359 (2017) 215–225.
[25] S. Goutam, J. Timmermans, N. Omar, P. Van Den Bossche, J. Van Mierlo, Comparative study of surface temperature behavior of commercial li-ion pouch cells of different chemistries and capacities by infrared thermography, energies 8 (2015) 8175–8192.
[26] J. Yi, U. Seong, C. Burm, T. Han, S. Park, Modeling the temperature dependence of the discharge behavior of a lithium-ion battery in low environmental temperature, J. Power Sources 244 (2013) 143–148.
[27] I. Bennion, J.A.R. Williams, L. Zhang, K. Sugden, N.J. Doran, UV-written in-fibre Bragg gratings, Opt. Quantum Electron. 28 (1996) 93–135.
[28] A. Raghavan, P. Kiesel, L. Sommer, J. Schwartz, A. Lochbaum, A. Hegyi, A. Schuh, K. Arakaki, B. Saha, A. Ganguli, K. Kim, C. Kim, H. Hah, S. Kim, G. Hwang, G. Chunag, B. Choi, M. Alamgir, Embedded fiber-optic sensing for accurate internal monitoring of cell state in advanced battery management systems part 1: cell embedding method and performance, J. Power Sources 341 (2017) 466–473.
[29] P. Wang, X. Zhang, L. Yang, X. Zhang, M. Yang, H. Chen, D. Fang, Real-time monitoring of internal temperature evolution of the lithium-ion coin cell battery during the charge and discharge process, Extrem. Mech. Lett. 9 (2016) 459–466.
[30] C. Lee, S. Lee, M. Tang, P. Chen, In situ monitoring of temperature inside lithium-ion batteries by flexible micro temperature sensors, Sensors 11 (2011) 9942–9950.
[31] C. Lee, S. Lee, Y. Chen, M. Chung, K. Han, In-situ monitoring of temperature and voltage in lithium-ion battery by embedded flexible micro temperature and voltage sensor, Int. J. Electrochem. Sci. 8 (2013) 2968–2976.
[32] G. Zhang, S. Ge, T. Xu, X.G. Yang, H. Tian, C.Y. Wang, Rapid self-heating and internal temperature sensing of lithium-ion batteries at low temperatures, Electrochim. Acta 218 (2016) 149–155.
[33] X.G. Yang, G. Zhang, C.Y. Wang, Computational design and refinement of self-heating lithium ion batteries, J. Power Sources 328 (2016) 203–211.
[34] G. Zhang, S. Ge, T. Xu, X. Yang, H. Tian, C. Wang, Rapid self-heating and internal temperature sensing of lithium-ion batteries at low temperatures, Electrochim. Acta 218 (2016) 149–155.
[35] S. Based, O.N. The, S. Effect, Sensors based on the seebeck effect, Sens. Actuat. 10 (1986) 321–346.
[36] S. Al Hallaj, H. Maleki, J.S. Hong, J.R. Selman, Thermal modeling and design considerations of lithium-ion batteries, J. Power Sources 83 (1999) 1–8.
[37] T. Amietszajew, E. McTurk, J. Fleming, R. Bhagat, Understanding the limits of rapid charging using instrumented commercial 18650 high-energy Li-ion cells, Electrochim. Acta 263 (2018) 346–352.
[38] A. Ganguli, B. Saha, A. Raghavan, P. Kiesel, K. Arakaki, A. Schuh, J. Schwartz, A. Hegyi, L. Sommer, A. Lochbaum, S. Sahu, M. Alamgir, Embedded fiber-optic sensing for accurate internal monitoring of cell state in advanced battery management systems part 2: internal cell signals and utility for state estimation, J. Power Sources 341 (2017) 474–482.
[39] X. Han, M. Ouyang, L. Lu, J. Li, Y. Zheng, Z. Li, A comparative study of commercial lithium ion battery cycle life in electrical vehicle: aging mechanism identification, J. Power Sources 251 (2014) 38–54.
[40] Y. Gao, J. Jiang, C. Zhang, W. Zhang, Z. Ma, Y. Jiang, Lithium-ion battery aging mechanisms and life model under different charging stresses, J. Power Sources 356 (2017) 103–114.
[41] A. Ukil, H. Braendle, P. Krippner, Distributed temperature sensing: review of technology and applications, IEEE Sens. J. 12 (5) (2012) 885–892.
[42] M.V. Klein, Optics, Wiley, New York, 1970.
[43] J. Song, W. Li, P. Lu, Y. Xu, L. Chen, X. Bao, Long-range high spatial resolution distributed temperature and strain sensing based on optical frequency-domain reflectometry, IEEE Photonics J 6 (3) (2014) 1–8.
[44] K. Yuksel, M. Wuilpart, V. Moeyaert, P. Mégret, Optical frequency domain reflectometry: a review, in: Ict. 2009 11th Int. Conf. Transparent Opt. Networks, 2009, pp. 3–7.
[45] E. Karamehmedovic, U. Glombitza, Fiber optic distributed temperature sensor using incoherent optical frequency domain reflectometry, Emerg. Optoelectron. Appl. 5363 (2004) 107.
[46] R. Passy, N. Gisin, J.P. von der Weid, H.H. Gilgen, Experimental and theoretical investigations of coherent OFDR with semiconductor laser sources, J. Light. Technol. 12 (9) (1994) 1622–1630.
[47] B.J. Soller, D.K. Gifford, M.S. Wolfe, M.E. Froggatt, High resolution optical frequency domain reflectometry for characterization of components and assemblies, Opt. Express 13 (2) (2005) 666.
[48] M. Froggatt, J. Moore, High-spatial-resolution distributed strain measurement in optical fiber with Rayleigh scatter, Appl. Opt. 37 (10) (1998) 1735–1740.
[49] D. Worwood, J. Marcos, Q. Kellner, H. Elham, R. McGlen, D. Mullen, K. Lynn, D. Greenwood, Experimental analysis of a novel cooling material for large format automotive lithium-ion cells, Energies 12 (7) (2019).